

A quantitative comparison of one-way extrapolation operators

Robert J. Ferguson
Department of Geological Sciences,
Campus mail code C1100,
University of Texas at Austin, USA.
E-mail: fergusonr@mail.utexas.edu

Abstract

In regions of strong lateral heterogeneity, the use of one-way wavefield extrapolators for seismic migration and modeling is a significant challenge. If high spatial resolution is required, computational cost becomes an immediate problem. If efficiency is desired, accuracy is sacrificed. Using a simple physical argument, we present a framework by which operators can be compared in terms of cost and accuracy, so that, for a fixed cost, the best operator can be selected during imaging/modeling depending on the complexity of the current level in the model.

As an example, two common wavefield extrapolation operators are derived from the Fourier integral operator of one-way wavefield extrapolation. One uses a desampling of the input velocity model so that the number of significant values in the extrapolation matrix is reduced, and an efficient implementation can be realized. The second is based on reducing the number of unique velocities in the model.

Using a simple physical argument, the two operators are compared in terms of accuracy and cost for two freely available velocity models. For the Marmousi model, where velocity variation tends to be blocky, the method based on reducing the number of unique velocities returns the greater accuracy for equivalent cost. For the Salt model, variation above and below the salt is smooth, the operator based on desampling the velocity field is more accurate for equivalent cost. At the level of the salt, however, we find that the reduced method returns greater accuracy.

Introduction

Seismic imaging can be generalized into two basic approaches *recursive extrapolation* and *direct inversion*. In direct inversion, the seismic image is produced by mapping the recorded seismic wavefield onto a model of the subsurface. Mathematically, imaging by direct inversion is based on the Born approximation to the inverse scattering problem (Bleistein et al., 2000). The reflection coefficient at a point in the subsurface is given by integrating the seismic data over a travelt ime surface defined by tracing raypaths from the subsurface point to the receiver locations. During integration, the data are multiplied by weights that are complex functions of recording geometry, the velocity field, and the orientation of the unknown reflector (Bleistein et al., 2000). Though a challenging computation, direct inversion typically requires less computational effort than recursive extrapolation (Bleistein et al., 2000). Direct inversion methods are computationally fast and flexible in their implementation but,

in their most basic form, they restrict wave propagation to a single Snell's law raypath between the subsurface location and a particular receiver (Gray, 2001).

In the recursive-extrapolation approach, the position and numerical value of a point in the subsurface is computed by cross-correlating the recorded wavefield with a model of the source after they have both been extrapolated recursively to that point. The recursive extrapolation process does not assume a particular Snell's law raypath. Rather, the cascade of very many extrapolation steps effectively honors all possible paths, not just the Snell's law path.

Imaging by recursive extrapolation can be generalized into two approaches: *one-way* and *two-way* operator based. Both methods use operators to predict wavefields at points in the subsurface. The latter uses a two-way solution to the wave equation resulting in the modeling of the entire propagating wavefield. With extremely accurate models of the elastic parameters of the subsurface, the two-way operators accurately mimic the propagation of all modes of seismic waves. If, however, the model is inaccurately known, the two-way methods generate spurious events that require sophisticated suppression techniques (Zhu and Lines, 1998).

One-way extrapolation operators are the subject of this paper, and they arise from an approximate solution to the wave equation. The solution is approximate in that lateral variation in elastic parameters is assumed to be weak such that the propagating wavefield doesn't generate scattered wavefields. One-way operators tend to be faster than two-way operators and slower than the direct-inverse methods. Also, they don't generate spurious events wherever contrasts in elastic parameters are found, and they naturally allow multiple wave arrivals at single points. In strongly heterogeneous media, however, accuracy is lost for paths that deviate by large angles from vertical.

In this paper, two operators will be derived directly from a Fourier integral operator of one-way wavefield extrapolation. Part of this derivation is similar to the development of the phase-screen operators (Wu and Huang, 1992, Le Rousseau and de Hoop, 2001) with the departure that a stationary, or space invariant, background velocity is not imposed. Extrapolation is then factored into the traditional focusing and differential thin-lens terms. Both terms, however, remain spatially variant, and the computational cost of applying the focusing term is large.

For efficiency, the focusing term is modified using two approaches. One approach results in the extended split step scheme of (Kessinger, 1992) where the phase-shift-plus-interpolation (PSPI) method (Gazdag and Sguazzero, 1984) is combined with the differential thin-lens term from the split-step method (Stoffa et al., 1990). When the focusing term is parameterized with the complete model, the result is identical to that of the Fourier integral operator. For a single reference velocity, the result is identical to the split-step operator. Parameterization intermediate to these extremes results in operators that balance accuracy and computational efficiency.

The second approach reduces computational cost by smoothing the velocity model laterally as in the generalized $\omega-k$ schemes of Pai (1998), Kosloff and Kessler (1987), and Benson (1995). Computationally, the resulting operator is applied as a matrix in the full Fourier domain where the nonzero terms are grouped around the trace. Efficiency is gained by computing and applying a restricted range on either side

of the trace of the matrix. When the entire range around the trace is used, the effective operator is identical to the Fourier integral operator. For a filter that passes only D.C., the effective operator is identical to the split-step operator (Stoffa et al., 1990).

For comparison, a simple expression is derived that relates error in the the resulting image with computational cost. Recognizing that error increases monotonically with phase angle, error is computed for a maximum phase angle, and RMS error is used to compare operators for a given velocity variation. This framework for analysis is used to determine which of the two operators is best suited for modeling/migration of two freely available velocity models - the Marmousi model and the SEG/EAGE Salt model.

Theory

Extrapolation of monochromatic seismic wavefield ψ from z at the surface to $z + \Delta z$ in the subsurface can be computed using Taylor series ((Margrave and Ferguson, 2000), Appendix A this paper) with the result:

$$\psi(\mathbf{x}, z + \Delta z, \omega) = \frac{1}{(2\pi)^2} \int \varphi(\mathbf{k}, z, \omega) \alpha(v(\mathbf{x}), \mathbf{k}, \Delta z) e^{-i\mathbf{k}\cdot\mathbf{x}} d\mathbf{k}, \quad (1)$$

where spectrum φ is the spatial 2D Fourier transform of ψ obtained at surface (\mathbf{x}, z)

$$\varphi(\mathbf{k}, z, \omega) = \frac{1}{(2\pi)^2} \int \psi(\mathbf{x}, z, \omega) e^{i\mathbf{k}\cdot\mathbf{x}} d\mathbf{x}, \quad (2)$$

and extrapolator α is given by

$$\alpha(v(\mathbf{x}), \mathbf{k}, \Delta z) = e^{i\Delta z k_z(v(\mathbf{x}), \mathbf{k})} \quad (3)$$

where \mathbf{k} is a wavenumber vector corresponding to \mathbf{x} . Wavenumber k_z corresponding to depth z is computed

$$k_z(\mathbf{x}, \mathbf{k}) = \begin{cases} \text{sgn}(\Delta z) \frac{\omega}{v(\mathbf{x})} \sqrt{1 - \frac{v(\mathbf{x}) \mathbf{k} \cdot \mathbf{k}}{\omega^2}} & \text{if } \frac{v(\mathbf{x}) \mathbf{k} \cdot \mathbf{k}}{\omega^2} \leq 1 \\ i \text{sgn}(\Delta z) \frac{\omega}{v(\mathbf{x})} \sqrt{1 - \frac{v(\mathbf{x}) \mathbf{k} \cdot \mathbf{k}}{\omega^2}} & \text{if } \frac{v(\mathbf{x}) \mathbf{k} \cdot \mathbf{k}}{\omega^2} > 1 \end{cases} \quad (4)$$

(sgn is the signum function).

Complex values of k_z correspond to the evanescent region where reflection energy is absent. In equation (4), we force complex values of k_z to be positive complex so that the resulting phase term $i\Delta z k_z$ in equation (1) is real valued and negative, and evanescent energy is forced to decrease exponentially.

Equation (2) extrapolates φ from surface (\mathbf{x}, z) to surface $(\mathbf{x}, z + \Delta z)$ simultaneously with a Fourier transform from \mathbf{k} to \mathbf{x} . It has a mathematical form identical to a Fourier integral operator (See for example books by Stein (1993) and Duistermaat (1995)).

Because the domain change in equation (1) is not strictly a Fourier transform, the fast Fourier transform algorithm cannot be used directly, and the computational effort

required for extrapolation is proportional to $M^2 N^2$, where M and N are the dimensions of the recording aperture. For example, given dimensions $M = N = 10^2$, the cost of extrapolating one monochromatic wavefield to a new depth requires 10^8 floating-point operations. For a model having 10^3 depths, the cost of extrapolation increases to 10^{11} calculations. For data with a few hundred frequencies of interest, the cost increases to 10^{13} calculations, and depending on the number of gathers, cost can increase orders of magnitude from there. Here it is worth noting that, even with this large computation load, equation (1) is still only an approximate solution to the wave equation.

Without loss of generality, introduce wavenumbers

$$\tilde{k}_z(\tilde{\nu}(\mathbf{x}), \mathbf{k}) = \frac{\omega}{\tilde{\nu}(\mathbf{x})} \sqrt{1 - \frac{\tilde{\nu}(\mathbf{x}) \mathbf{k} \cdot \mathbf{k}}{\omega^2}} \quad (5)$$

where $\tilde{\nu}(\mathbf{x}) \neq \nu(\mathbf{x})$ so that extrapolation symbol α (equation (3)) becomes

$$\alpha(\mathbf{x}, \mathbf{k}, \Delta z) = e^{i \Delta z \tilde{k}_z(\mathbf{x}, \mathbf{k})} e^{\left[\frac{\omega}{\tilde{\nu}(\mathbf{x}) \tilde{k}_z(\mathbf{x}, \mathbf{k}) \sqrt{1 - \left(\frac{\tilde{\nu}(\mathbf{x}) \mathbf{k} \cdot \mathbf{k}}{\omega^2} \right)^2}} - 1 \right]}. \quad (6)$$

Expand the phase of the second exponential term in equation (6) about $\mathbf{k} \cdot \mathbf{k} = 0$, and truncate to zero order to get

$$\tilde{\alpha}(\mathbf{x}, \mathbf{k}, \Delta z) = e^{i \Delta z \tilde{k}_z(\mathbf{x}, \mathbf{k})} e^{i \Delta z \omega \left[\frac{1}{\tilde{\nu}(\mathbf{x})} - \frac{1}{\nu(\mathbf{x})} \right]}. \quad (7)$$

Replacement of α in equation (1) with $\tilde{\alpha}$ above gives

$$\psi(\mathbf{x}, z + \Delta z, \omega) \approx \tilde{\psi}(\mathbf{x}, z + \Delta z, \omega) e^{i \Delta z \omega \left[\frac{1}{\tilde{\nu}(\mathbf{x})} - \frac{1}{\nu(\mathbf{x})} \right]}, \quad (8)$$

where

$$\tilde{\psi}(\mathbf{x}, z + \Delta z, \omega) = \frac{1}{(2\pi)^2} \int \varphi(\mathbf{k}, z, \omega) e^{i \Delta z \tilde{k}_z(\tilde{\nu}(\mathbf{x}), \mathbf{k}, \omega)} e^{-i \mathbf{k} \cdot \mathbf{x}} d\mathbf{k}. \quad (9)$$

For $\tilde{\nu} = \text{mean}\{\nu\}_x$, equation (8) is identical to the split-step Fourier operator (Stoffa et al., 1990). For $\tilde{\nu} = \nu$, equation (8) is identical to the Fourier integral operator in equation (1). Careful selection of $\tilde{\nu}$ intermediate to ν and $\bar{\nu}$ provides an operator that is potentially more accurate than the split-step operator and, if $\tilde{\nu}$ varies more slowly than ν , more amenable to approximate computation schemes that save cost while maintaining accuracy. We will refer to the the wavefield $\tilde{\psi}$ as the focused wavefield, and we will refer to the the complex exponential in equation (8) as the differential thin-lens term.

In the next sections, two specific operators from the infinite family implied by equation (1) will be derived that implement equation (8) efficiently.

Generalized $\omega-k$

By desampling the velocity field in the lateral coordinates, we arrive at an extrapolation operator that requires fewer computations than the equivalent operator

applied in the space domain (Pai, 1998, Kosloff and Kessler, 1987, Benson, 1995).

The Fourier transform $\mathbf{x} \rightarrow \mathbf{l}$ of equation (8) is

$$\tilde{\varphi}(\mathbf{l}, z + \Delta z, \omega) = \frac{1}{(2\pi)^2} \int \varphi(\mathbf{k}, z, \omega) A(\mathbf{k}, \mathbf{l}, \omega) d\mathbf{k}d\mathbf{l}, \quad (10)$$

where

$$A(\mathbf{k}, \mathbf{l}, \omega) = \int e^{i\Delta z k_z (\tilde{v}(\mathbf{x}, \mathbf{k}, \omega))} e^{-i\mathbf{x} \cdot [\mathbf{l} - \mathbf{k}]} d\mathbf{x}. \quad (11)$$

If \tilde{v} is chosen such that

$$\tilde{v}(\mathbf{x}) = (f * v)(\mathbf{x}) \quad (12)$$

where $*$ denotes convolution, and f is a high-cut filter, the number of discrete samples in the extrapolation symbol is reduced from $M \times N$, to $(m < M) \times (n < N)$ thereby reducing overall cost. Inverse Fourier transform $\mathbf{l} \rightarrow \mathbf{x}$ completes this first alternative calculation of the focused wavefield $\tilde{\psi}$ of equation (9). Complete extrapolation is then accomplished by applying the differential thin-lens term with equation (8).

The cost of implementing equation (8) with the low-cut filtered version of the velocity is $\propto mn[M \log_2 m + N \log_2 n]$ to compute A , plus $M N m n$ to apply A , plus $2 \times M N \log_2 M N$ for the Fourier transforms from space to wavenumber and back.

Figure 1 gives a simple example of fast wavefield extrapolation using a desampled version of the given velocity. A flat horizon is extrapolated 200m through the velocity field in Figure 1a. The true velocity is plotted along with the desampled version (dashed line). The focused wavefield, computed with this Fourier alternative to equation (8) is given in Figure 1b. A differential thin-lens term is then applied to correct the vertically collimated components of the wavefield to match approximately the true traveltimes (Figure 1c).

Figure 2 shows two sample extrapolation operators for a central frequency of 30 Hz corresponding to equation (11) parameterized with the velocity functions of Figure 1a. (The operators are the discrete equivalents of the analytic form of equation (11). They are applied to a single frequency of the wavefield with a matrix-vector multiplication.) Figure 2a is the operator corresponding to the true velocity, and Figure 2b is the operator corresponding to the smoothed velocity. The operator in Figure 2b has fewer significant non-zero terms compared to the operator in 2a and is less expensive to compute and apply.

Extended split step

An alternative to desampling the wavefield and applying a narrow operator in the frequency domain is to reduce the number of unique velocities in the lateral coordinates. This approach is identical to the extended split step method of (Kessinger, 1992). For $\tilde{v} = \lambda \times \text{round}(v/\lambda)$, where $\lambda \leq \min(v)$, the number of unique velocities p in \tilde{v} is

$$p = \frac{\max(\tilde{v}) - \min(\tilde{v})}{\lambda}. \quad (13)$$

In a procedure analogous to the PSPI method (Gazdag and Sguazzero, 1984, Kessinger, 1992), equation (8) becomes (Margrave and Ferguson, 2000)

$$\tilde{\psi}(\mathbf{x}, z, \omega) = \sum_{j=1}^p \Omega_j(\mathbf{x}) \frac{1}{(2\pi)^2} \int \varphi(\mathbf{k}, z, \omega) e^{i\Delta z k_z(v_j, \mathbf{k}, \omega) - i\mathbf{k} \cdot \mathbf{x}} d\mathbf{k}, \quad (14)$$

where Ω_j is a windowing function defined by

$$\begin{aligned} \Omega_j(\mathbf{x}) &= 1, \tilde{v}(\mathbf{x}) = v_j \\ &= 0, \tilde{v}(\mathbf{x}) \neq v_j. \end{aligned} \quad (15)$$

Equation (14) constructs p reference wavefields using constant velocity phase shift to extrapolate φ for each \tilde{v}_j . Windows Ω_j are computed and applied to select data from each reference wavefield at the locations where the reference velocity equals the desired velocity, and the resulting wavefields are superimposed. Unlike PSPI, no interpolation is used. The cost of implementing equation (8) with the focusing operator in equation (14) is $\propto p$ times the cost $MN \log_2 MN$ of the 2D FFT plus the 2D FFT of the input wavefield.

Figure 3 gives a simple example of fast wavefield extrapolation using a version of the given velocity that has been rounded to the nearest 200m/s so that the number of unique velocities is reduced laterally. (A good alternative to simply rounding velocities is to use the method of Bagaini et al. (1995).) A flat horizon is extrapolated 200m through the velocity field in Figure 3a. The true velocity is plotted along with the reduced version (dashed line). The extrapolated output is given in Figure 3b. A differential thin-lens correction is then used to correct the normal incidence components of the wavefield to match approximately the true traveltime (Figure 3c).

Focusing error

Given a fairly accurate velocity model, lateral positioning error is due to extrapolation operators that are approximate in some way. To compare the operators described in the previous sections, we will assume that the given velocity model is accurate and use a simple geometric relation to relate imaging error and computational cost.

From Figure 4, x is the lateral distance covered by a wave incident at angle θ from the vertical when it is extrapolated distance Δz through a velocity model. The geometric relationship between x , Δz and θ is:

$$x = \Delta z \tan(\theta), \quad (16)$$

or, in terms of velocity v and slowness p

$$x = \frac{\Delta z p v}{\sqrt{1 - (p v)^2}}. \quad (17)$$

The two operators described previously achieve computational efficiency by simplifying the velocity model, and $\Delta v = v_{true} - v_{simple}$ is the resulting velocity error.

To first order, the normalized error in x as a function of v is:

$$\frac{\Delta x}{x} \approx \frac{1}{x} \frac{\partial x}{\partial v} \Delta v$$

$$= \frac{\Delta v}{v} \frac{1}{\sqrt{1-(pv)^2}} = \frac{\Delta v}{v} \frac{1}{\cos(\theta)}. \quad (18)$$

We have then, from equation (18), normalized error in velocity $\Delta v/v$ and normalized error $\Delta x/x$ in position are related by the cosine of the propagation angle θ

$$\frac{\Delta v}{v} \approx \frac{\Delta x}{x} \cos(\theta). \quad (19)$$

For fixed velocity error, positioning error increases with propagation angle, becoming infinite at 90 degrees.

For a desired accuracy given as a percentage, and a maximum desired propagation angle, a percentage error in velocity is given by equation (19). This percentage then dictates how much the simplified velocity can deviate from the true velocity. For the method based on desampling the velocity field, a minimum Nyquist frequency is implied. For extended split step, a minimum number of unique velocities is implied. Then, at every depth, the decision to use one operator over another can be made based on balancing cost and accuracy.

Comparisons

Synthetic data sets are useful for demonstrating new technologies in seismic imaging. To compare the generalized $\omega-k$ operator and the extended split step operator, the Marmousi model (Bourgeois et al., 1991), and the SEG/EAGE salt model (Aminzadeh et al., 1996) are used. Impulses are forward modeled by extrapolation through each velocity field to a specific time when an image of the wavefield in space is computed. Contours derived from first-arrival eikonal raytracing are plotted to provide reference. In each example, the velocity fields are modified so each operator requires equivalent computational cost, and the resulting positioning error ($\Delta x/x$) is analyzed according to equation (19).

In 2D, the operator based on a desampled model (equation 10) has a computational cost c_d given by

$$c_d = mM \log_2 m + M m + 2M \log_2 M \quad (20)$$

where M is the number of inline traces and m is the number of samples in the inline direction of the velocity field. For the operator based on the reduced model (equation 14), computational cost c_r is computed using

$$c_r = [p+1]M \log_2 M, \quad (21)$$

where p is the number of unique velocities in the lateral direction.

Marmousi model

The Marmousi model (Bourgeois et al., 1991) is a synthetic seismic model suitable for testing imaging algorithms in 2D. The corresponding P-wave velocity (Figure 5) represents a profile through the Cuaza basin offshore Angola.

For extended split step, the model is rounded so the result (Figure 6) has $p=10$

unique velocity values along the lateral coordinate and, for $M = 512$ traces, the computational cost is proportional to $11 \times 512 \times \log_2 512 \approx 50000$ complex floating point operations. Figure 7 shows the positioning error associated with Figure 6. Intensities represent absolute value of positioning error in percent for waves incident at 45 degrees. (The value of 45 degrees is arbitrarily selected as the highest propagation angle of importance in this example.) Error is restricted to $\pm 15\%$, with the largest error associated with the features to the right and left of the anticline (between 1500m and 2500m depth).

For generalized $\omega-k$, the Marmousi model is low-pass filtered so that the spatial Nyquist frequency is reduced so that $m = 8$. The smoothed result is given in Figure 8. For wavefield extrapolation using equation (10), cost is proportional to $8 \times 512 \times \log_2 16 + 512 \times 8 + 512 \times \log_2 512 \approx 50000$. Figure 9 is a plot of the focusing error associated with Figure 8. Error varies between 60% and -140%, and is much larger in most parts of the model than the error associated with the reduced model.

In Figure 10a, the focusing errors in Figures 7 and 9 are averaged over the lateral coordinates and plotted as functions of depth. Again, for most depths, average error is larger for the desampled model. The greatest difference occurs at 1260m and the full velocity profile is plotted in Figure 10b. The reduced velocity tracks most of the variation apparent in the true velocity, while the desampled velocity is a very smooth approximation. At 2020m, however, the average error associated with the reduced velocity is larger: Figure 10c shows the corresponding velocity profile and, though the reduced velocity tracks most of the true velocity, significant departures occur between 0m and 4200m distance. The desampled velocity tracks faithfully through this region, hence returns greater accuracy.

Figures 11 and 12 show comparisons of forward modeling of source impulses using the extended split step and generalized $\omega-k$ respectively. The location of the source is distance 4670m and depth 195m, and the elapsed time is 0.82ms. In these Figures, the differential thin-lens correction is not included. For comparison, the corresponding contour from a traveltimes map of Figure 5 is plotted as well as the normal incidence reflectivity. The contour represents first arrival traveltimes as computed using an eikonal-solver, and head waves are present.

The wavefield in Figure 11 tracks the first-arrival contour more accurately than in Figure 12. Head waves should not be generated by these one-way operators and this can be seen by the absence of wave energy tracking the contour corresponding to headwaves on the left side of both Figures. Some leakage of energy from the evanescent region is visible in Figure 12.

In Figures 13 and 14, the differential thin-lens correction has been applied. The corrected wavefield corresponding to the extended split-step operator (Figure 13) is not significantly different than the uncorrected wavefield (Figure 11) owing to the accuracy of the focused wavefield alone. Figure 14 shows significant improvement when the differential thin-lens correction is applied, though higher dips are not well represented. Both operators, however, are an improvement over the split-step method (the focusing term is computed with a single value for velocity), in Figure 15. It is clear that for a $\sim 6\times$ increase in cost relative to the split-step method, the extended

split-step and generalized $\omega-k$ methods provide superior results.

SEG salt model

The Seg/EAGE Salt model (Aminzadeh et al., 1996) in Figure 16 represents a salt body embedded in smoothly varying sediments in the Gulf of Mexico. Because of the smoothness of the model above and below the salt, it is expected that generalized $\omega-k$ would have great utility as the reduced model may to coarsely represent a smooth variation.

For extended split step, the model is rounded so that the reduced model (Figure 17) has $p=10$ (equation 21) unique velocities. For $M=1024$ traces, the computational cost is proportional to $11 \times 1024 \times \log_2 1024 \approx 110000$ complex floating point operations. Figure 18 shows the error associated with Figure 17, and varies between $\pm 25\%$. The largest error is associated with the sediments on either side of the salt.

For generalized $\omega-k$, the model is low-pass filtered so that the spatial Nyquist frequency is reduced by a factor of $8/1024$ where $m=8$. The smoothed result is given in Figure 19. Here, the cost of generalized $\omega-k$ is proportional to $8 \times 1024 \times \log_2 8 + 1024 \times 8 + 1024 \times \log_2 1024 \approx 110000$, and Figure 20 is a plot of the focusing error associated with Figure 19. Error varies between 55% and -250% , and is again much larger in most parts of the model than the error associated with the reduced model.

In Figure 21a, the focusing errors in Figures 18 and 20 are averaged over the lateral coordinates and plotted as functions of depth. At levels related to the salt, average error is larger for the desampled model. Above and below the salt in the smoothly varying sediments, generalized $\omega-k$ returns slightly greater accuracy. Similarly, near the top of the salt at 2160m depth. The full profile is plotted in Figure 21b. The reduced velocity tracks the velocity spike corresponding to distance 6000 and poorly tracks the smooth variation of the sedimentary velocities. The desampled velocity misses the spike, but readily tracks the sediment velocity. (Included in the original velocity model are numerous velocity spikes present to excite diffraction in forward modeling. For the purposes here, these spikes are removed using a short median filter. Also, the model is interpolated to increase the number of traces from 676 to 1024 traces. An anti-alias filter was applied resulting in some Gibbs noise at strong velocity contrasts.) In the salt, the average error associated with extended split step is much less than for generalized $\omega-k$ in particular at 2160m depth (Figure 21).

Figures 22 and 23 show comparisons of forward modeling of source impulses using the focusing operators from extended split step and generalized $\omega-k$ respectively. The location of the source is distance 6000m and depth 1000m, and the elapsed time is 0.588ms.

The wavefield in Figure 22 tracks the first arrival contour more accurately than in Figure 23.

In Figures 24 and 25, the differential thin-lens correction has been applied. Again, the corrected wavefield corresponding to extended split step (Figure 24) is not

significantly different than the uncorrected wavefield (Figure 22) (the focusing term is accurate), and Figure 25 is significantly improved. Kinematically, both methods are an improvement over the phase-screen method (Figure 26), though the evanescent leakage from the generalized $\omega - k$ operator is causing amplitude growth.

Conclusions

I use a general description of one-way extrapolation to relate the cost and accuracy of two different one-way extrapolation operators. I demonstrate that, because computational cost is proportional to the cost of the fast Fourier transform for most operators, and because imaging error is related to phase error, cost and accuracy have a simple relationship. To provide a physically meaningful basis for analysis, I relate phase error to error in lateral position. This results in an efficient framework from which selection of operators for imaging can be tailored to each depth interval in a model.

Acknowledgments

The author wishes to thank Dr. Sergey Fomel of the Bureau of Economic Geology, University of Texas, Austin for providing the travel-time contours used in this work. I also thank the Exploration Development Geophysics Education and Research (EDGER) Forum, University of Texas, Austin for supporting this work.

Bibliography

Aminzadeh, F., Burkhard, N., Long, J., Kunz, T., and P. Duclos, 1996, Three dimensional SEG/EAGE models - An update: The Leading Edge, 15, 02, 131-134.

Bagaini, C., Bonomi, E., and Pieroni, E., 1995, Data parallel implementation of 3-D PSPI: Soc. of Expl. Geophys., 65th Ann. Internat. Mtg, 188-191.

Benson, A. K., 1995, Phase-shift migration with a variable-length spatial transform - An algorithm for moderately varying lateral velocities, Geophys. Prosp., 43, 06, 729-741.

Bleistein, N., and J. K. Cohen, J. K., and Stockwell, J. W.", 2000, Mathematics of multidimensional seismic imaging, migration, and inversion, Springer.

Bourgeois, A., Bourget, M., Lailly, P., Poulet, M., Ricarte, P., and Versteeg, R., 1991, Marmousi model and data: The Marmousi experience, Euro. Assn. of Geosci. and Eng., R Versteeg and G Gram, 5 - 9.

Duistermaat, J. J., 1995, Fourier integral operators: Springer-Verlag.

Gray, S. H., 2001, Seismic imaging: Geophysics, Soc. of Expl. Geophys., 66, 1, 15-17.

Gazdag, J., and P. Sguazzero, P., 1984, Migration of seismic data by phase-shift plus interpolation: Geophysics, 49, 02, 124-131.

Kessinger, W., 1992, Extended split-step Fourier migration: Soc. of Expl. Geophys., 62nd Ann. Internat. Mtg, 917-920.

Kosloff, D., and Kessler, D., 1987, Accurate depth migration by a generalized phase-shift method, Geophysics, 52, 08, 1074-1084.

Le Rousseau, J. H., and M. V. de Hoop, 2001, Modeling and imaging with the scalar generalized-screen algorithms in isotropic media: Geophysics, 66, 5, 1551-1568.

Margrave, G. F., and Ferguson, R. J., 1999, Wavefield extrapolation by nonstationary phase shift: Geophysics, 64, 4, 1067-1078.

Margrave, G. F., and Ferguson, R. J., 2000, Taylor series derivation of nonstationary wavefield extrapolators, Soc. of Expl. Geophys., 70th Ann. Internat. Mtg, 834-837.

Pai, D. M., 1988, Generalized f-k (frequency-wavenumber) migration in arbitrarily varying media: Geophysics, 53, 12, 1547-1555.

Stein, E. M., 1993, Harmonic analysis: real-variable methods, orthogonality, and oscillatory integrals: Princeton University Press.

Stoffa, P. L., Fokkema J. T., de Luna Freire, R. M., and W. P. Kessinger, 1990, Split-step Fourier migration: Geophysics, 55, 04, 410-421.

Wu, R. S., and Huang, L. Y., 1992, Scattered field calculation in heterogeneous media using phase-screen propagation, Soc. of Expl. Geophys., 62nd Ann. Internat. Mtg, 1289-1292.

Zhu, J., and Lines, L., 1998, Comparison of Kirchhoff and reverse-time migration methods with applications to prestack depth imaging of complex structures, Geophysics, 63, 04, 1166-1176.

Appendix A

Extrapolation of wavfield φ from z at the surface to $z + \Delta z$ in the subsurface can be computed using Taylor series:

$$\psi(\mathbf{x}, z + \Delta z, \omega) = \sum_{|\alpha| \leq \infty} \frac{(\Delta z)^\alpha}{\alpha!} \partial_z^\alpha \psi(\mathbf{x}, z, \omega). \quad (\text{A1})$$

To obtain the required partial derivatives $\partial_z^\alpha \psi$, we note that the acoustic wave equation provides an exact expression for $\partial_z^2 \psi$ (Kessinger, 1992):

$$\partial_z^2 \psi(\mathbf{x}, z, \omega) = \frac{1}{(2\pi)^2} \int e^{i\mathbf{x} \cdot \mathbf{k}} k_z^2 (v(\mathbf{x}), \mathbf{k}, \omega) \varphi(\mathbf{k}, z, \omega) d\mathbf{k}, \quad (\text{A2})$$

where k_z is given in equation (4).

From equation (A2), the following inference is made

$$k_z^\alpha(v(\mathbf{x}), \mathbf{k}, \omega) \approx \left[\left(\frac{\omega}{v(\mathbf{x})} \right)^2 - \mathbf{k} \cdot \mathbf{k} \right]^{\frac{\alpha}{2}}, \quad (\text{A3})$$

and a general expression is obtained:

$$\partial_z^\alpha \psi(\mathbf{x}, z, \omega) \approx \frac{1}{(2\pi)^2} \int e^{i\mathbf{x} \cdot \mathbf{k}} (ik_z)^\alpha (v(\mathbf{x}), \mathbf{k}, \omega) \varphi(\mathbf{k}, z, \omega) d\mathbf{k}. \quad (\text{A4})$$

If the physical properties of the Earth represented by k_z can be estimated, wavefield $\psi(\mathbf{x}, z + \Delta z)$ can be computed using equations (A1) and (A4):

$$\psi(\mathbf{x}, z + \Delta z, \omega) = \frac{1}{(2\pi)^2} \int e^{i\mathbf{x} \cdot \mathbf{k}} \varphi(\mathbf{k}, z, \omega) \sum_{|\alpha| \leq \infty} \frac{(\Delta z)^\alpha}{\alpha!} i^\alpha k_z^\alpha (v(\mathbf{x}), \mathbf{k}, \omega) d\mathbf{k}. \quad (\text{A5})$$

Recognizing the series expansion for e^x we have the result:

$$\psi(\mathbf{x}, z + \Delta z, \omega) = \frac{1}{(2\pi)^2} \int e^{i\mathbf{x} \cdot \mathbf{k}} e^{i\Delta z k_z(v(\mathbf{x}), \mathbf{k}, \omega)} \varphi(\mathbf{k}, z, \omega) d\mathbf{k}. \quad (\text{A6})$$

Inverse Fourier transform $\omega \rightarrow t$ of equation (A6) completes extrapolation.

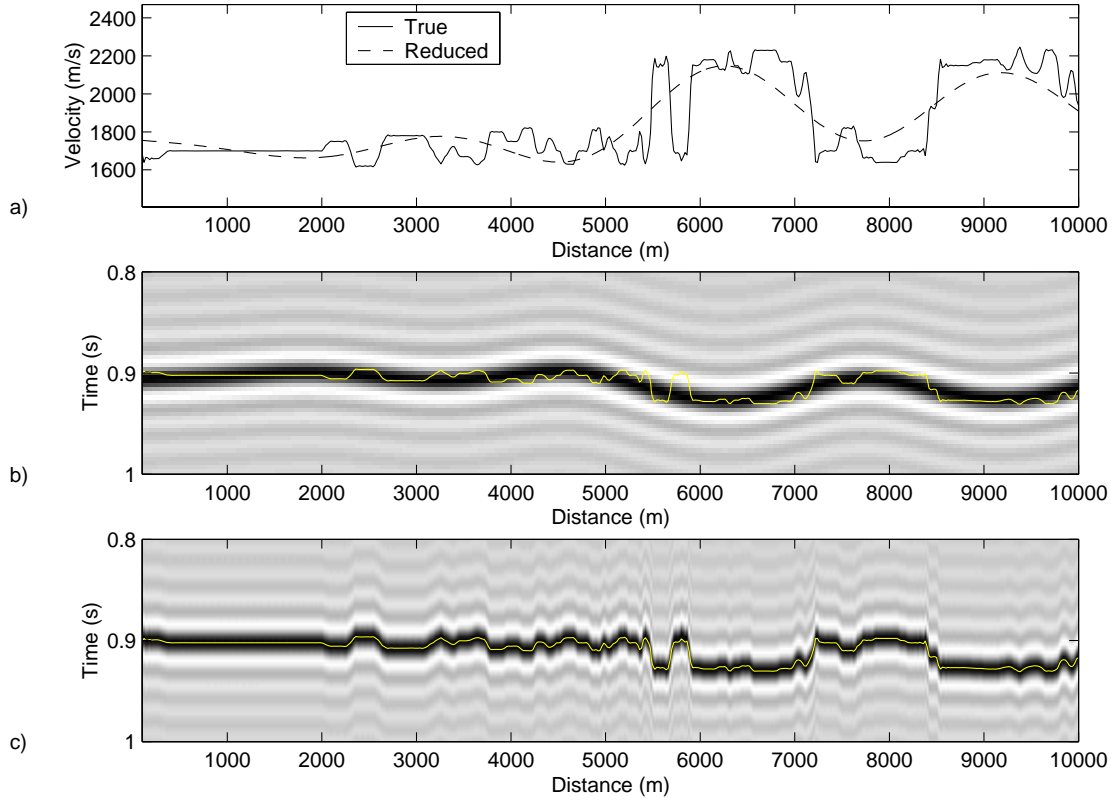


Figure 1. A flat horizon is extrapolated through a laterally variable velocity field using equation (10) parameterized with a smoothed version of the velocity. a) The true velocity and the smoothed version. b) Extrapolation output using equation (10). The correct travel times are plotted in gray. c) The wavefield of Figure (b) corrected with the the differential thin-lens term. This example is about twice as expensive to compute as the example in Figure 3.

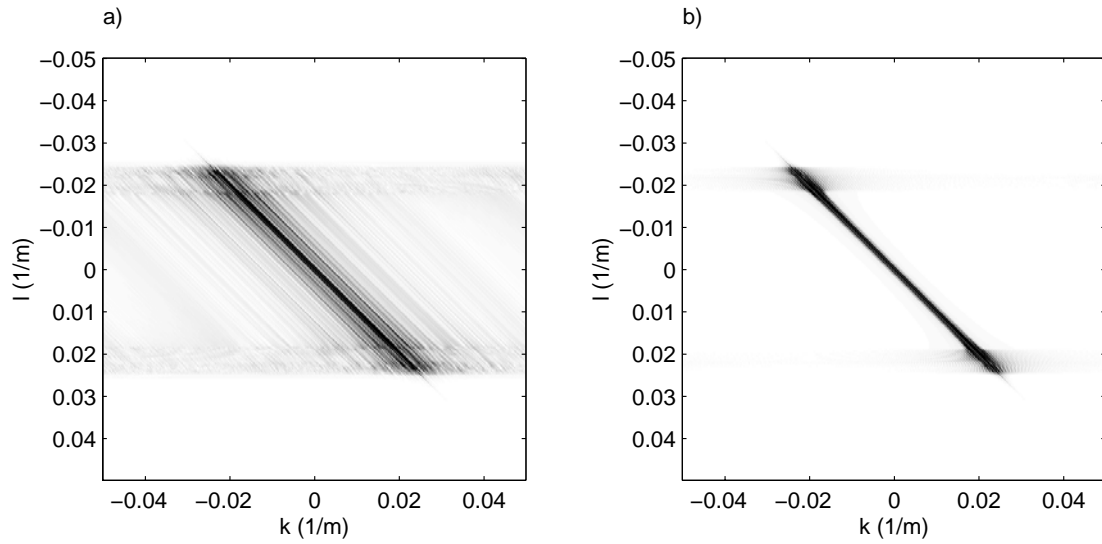


Figure 2. Fourier extrapolation operators (equation 11). a) The Fourier operator is parameterized with the true velocity given in Figure 2(a) (solid curve). b) The operator parameterized with the smooth velocity (dashed curve). The operator in (b) has far fewer non-zero terms than (a) and is much less expensive to compute and apply.

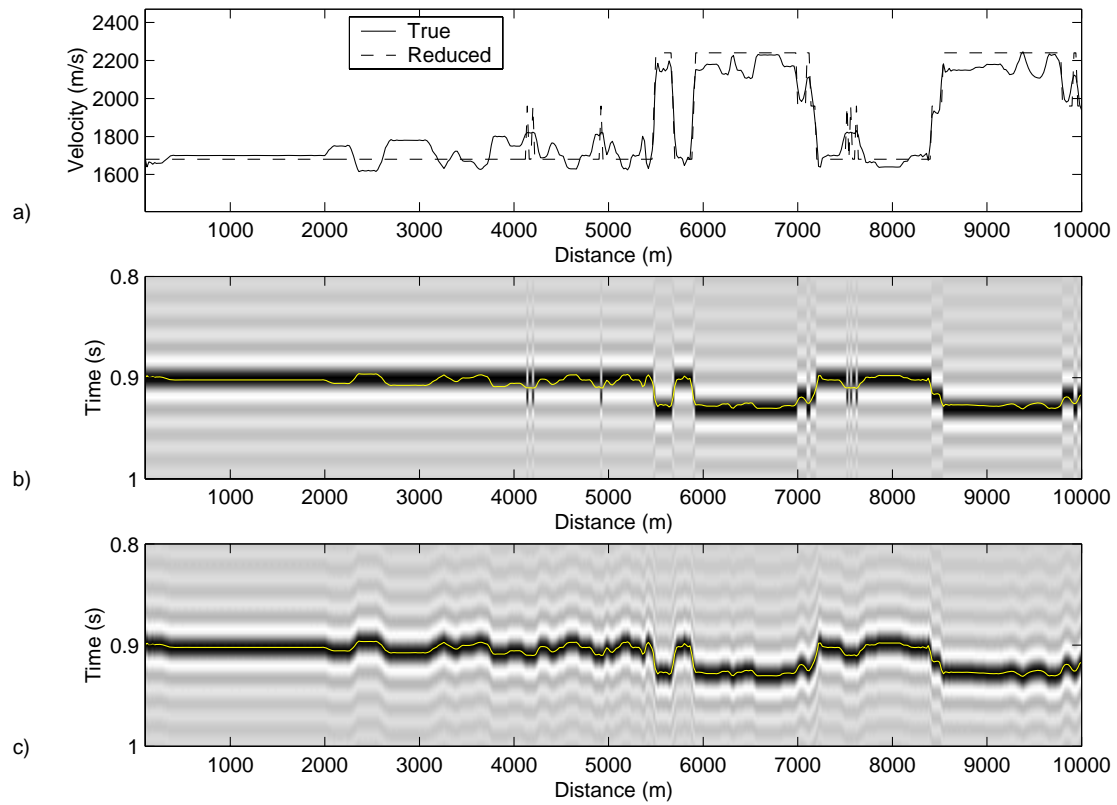


Figure 3. A flat horizon is extrapolated through a laterally variable velocity field using equation (14) parameterized with a blocky version of the velocity. The true velocity (solid) and a smoothed version (dashed). b) Extrapolation output. The correct travel times are plotted in gray. c) The wavefield of Figure (b) corrected with the the differential thin-lens term. This example is about half as expensive to compute as the example in Figure 1.

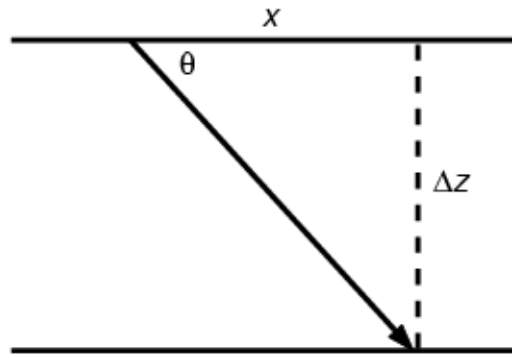


Figure 4. Illustration of a wave incident at an angle θ measured from horizontal.

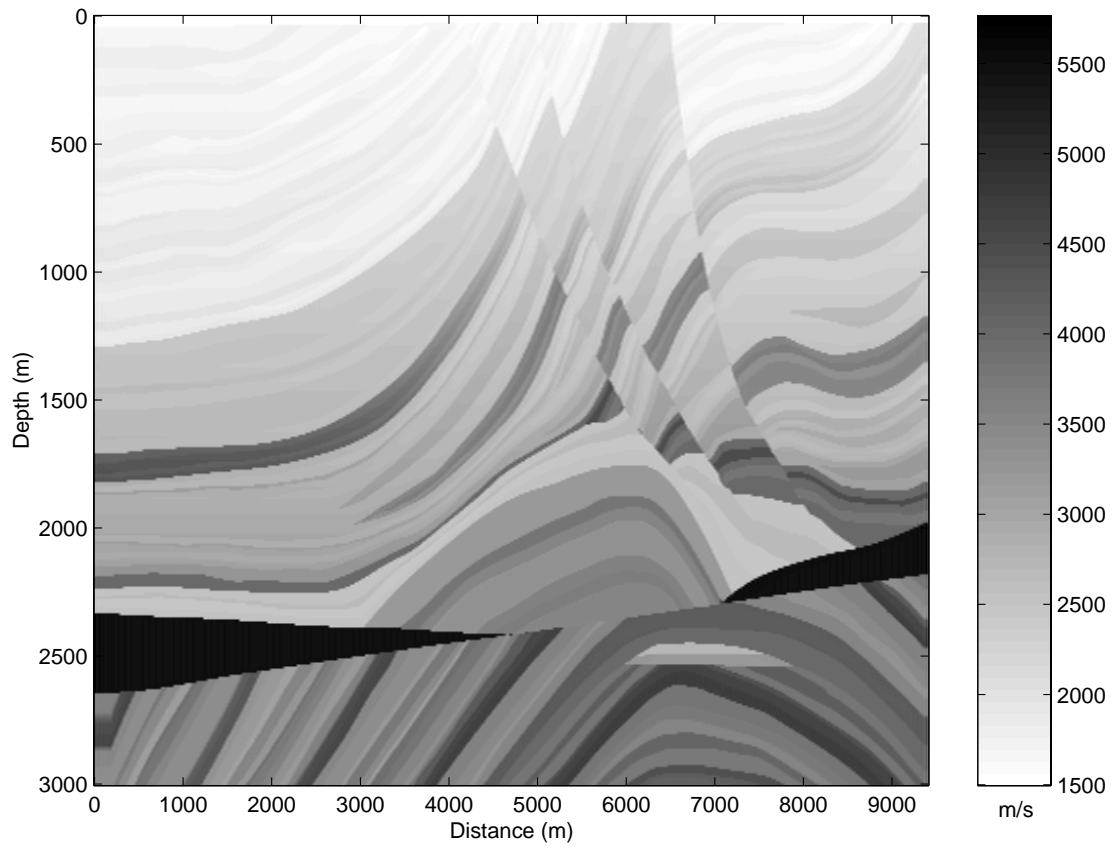


Figure 5. Marmousi velocity model.

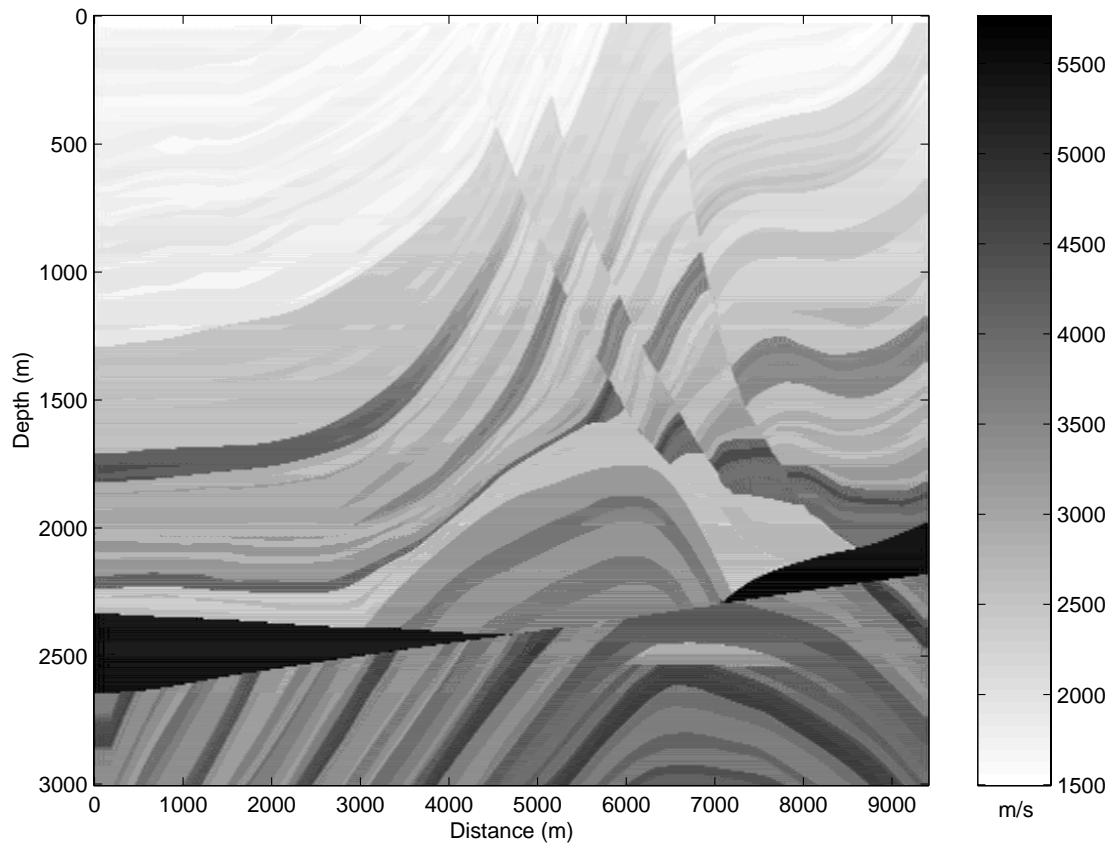


Figure 6. The Marmousi model reduced to 10 unique velocity values along the lateral coordinate. This velocity profile is used to generate the impulse response in Figures 11 and 13.

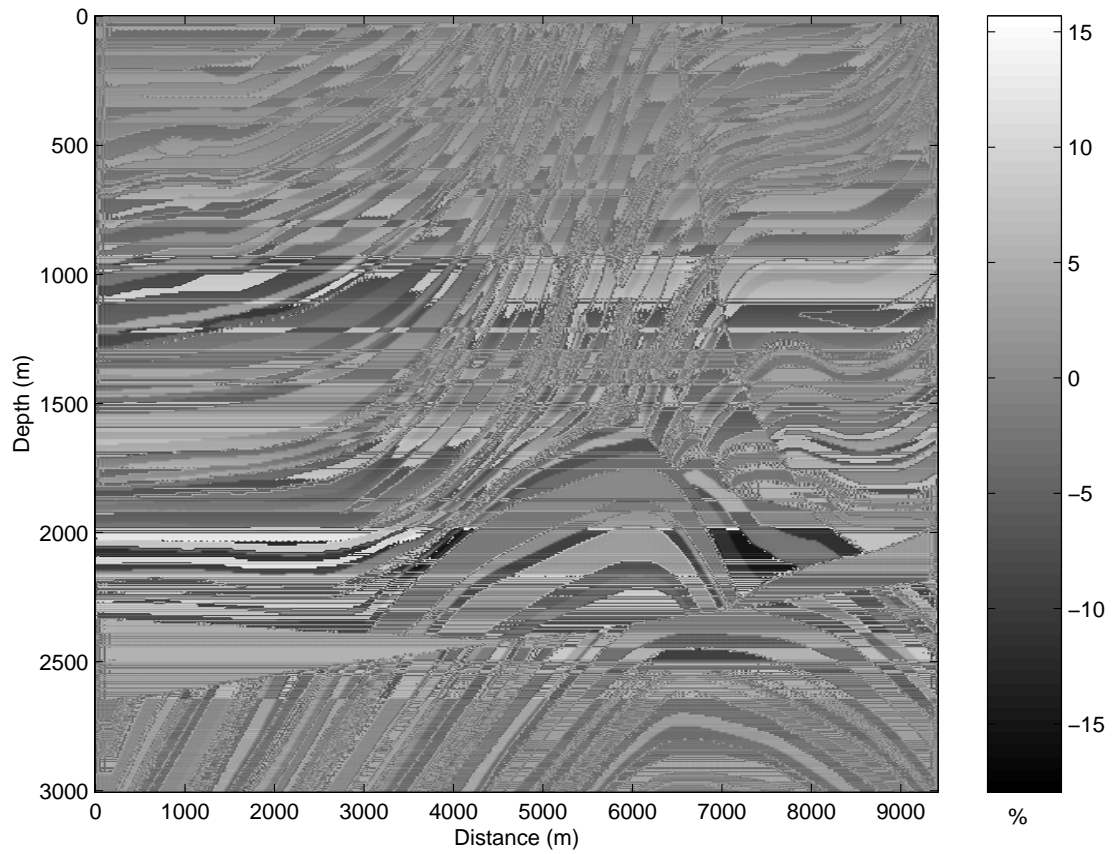


Figure 7. Positioning error associated with the reduced model of Figure 6. Intensities represent absolute value of positioning error in percent for waves incident at 45 degrees.

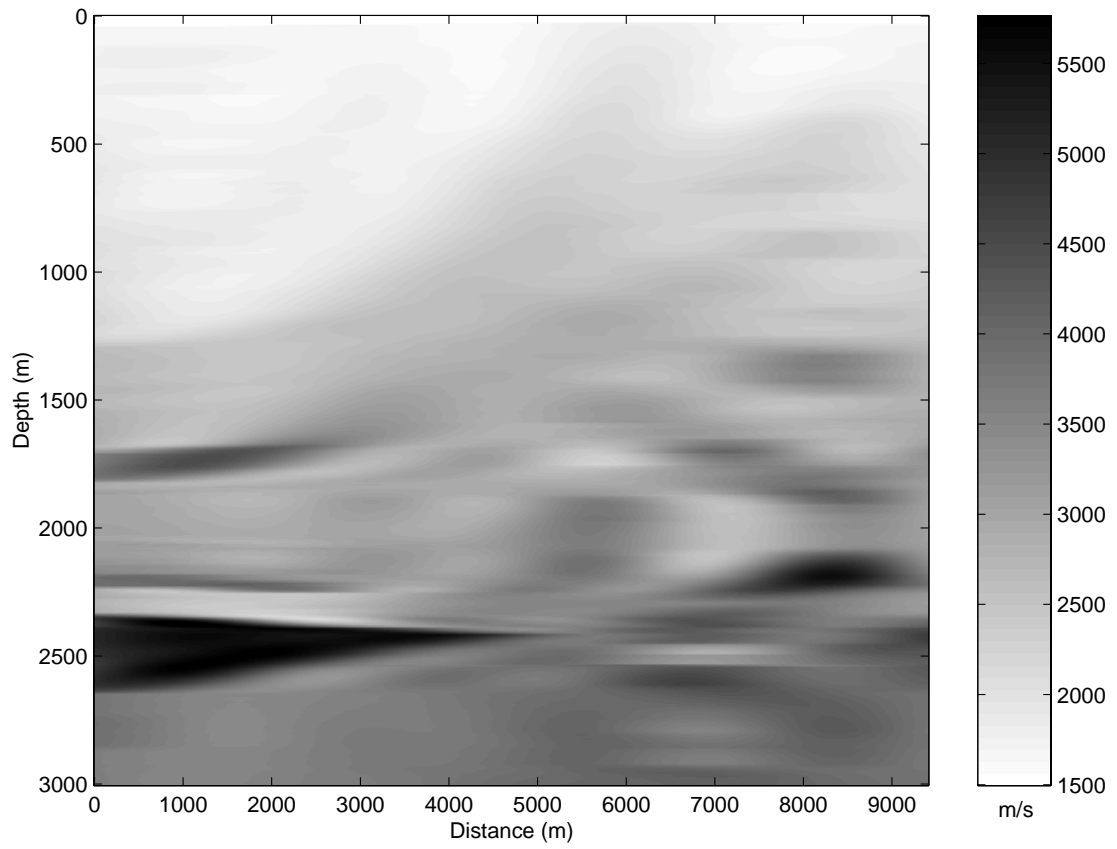


Figure 8. The Marmousi model desampled to 8 velocity values along the lateral coordinate. This velocity profile is used to generate the impulse response in Figures 12 and 14.

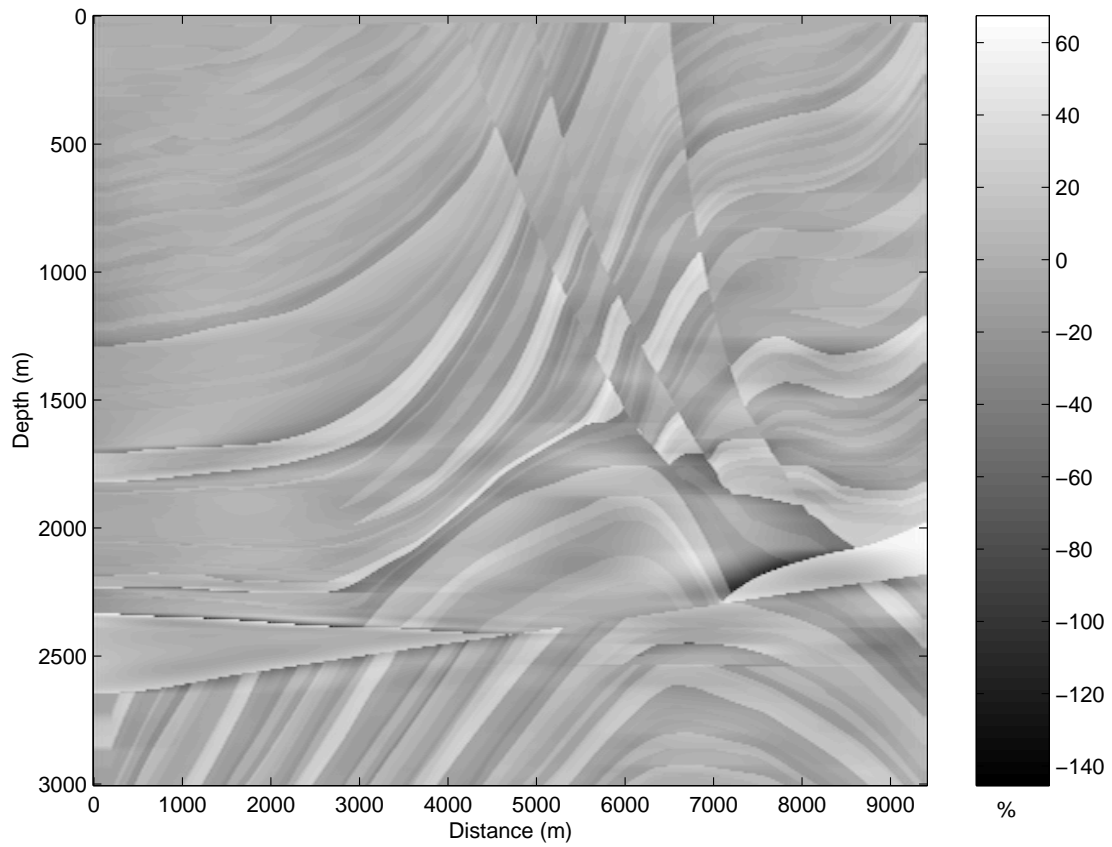


Figure 9. Positioning error associated with the desampled model of Figure 8. Intensities represent absolute value of positioning error in percent for waves incident at 45 degrees.

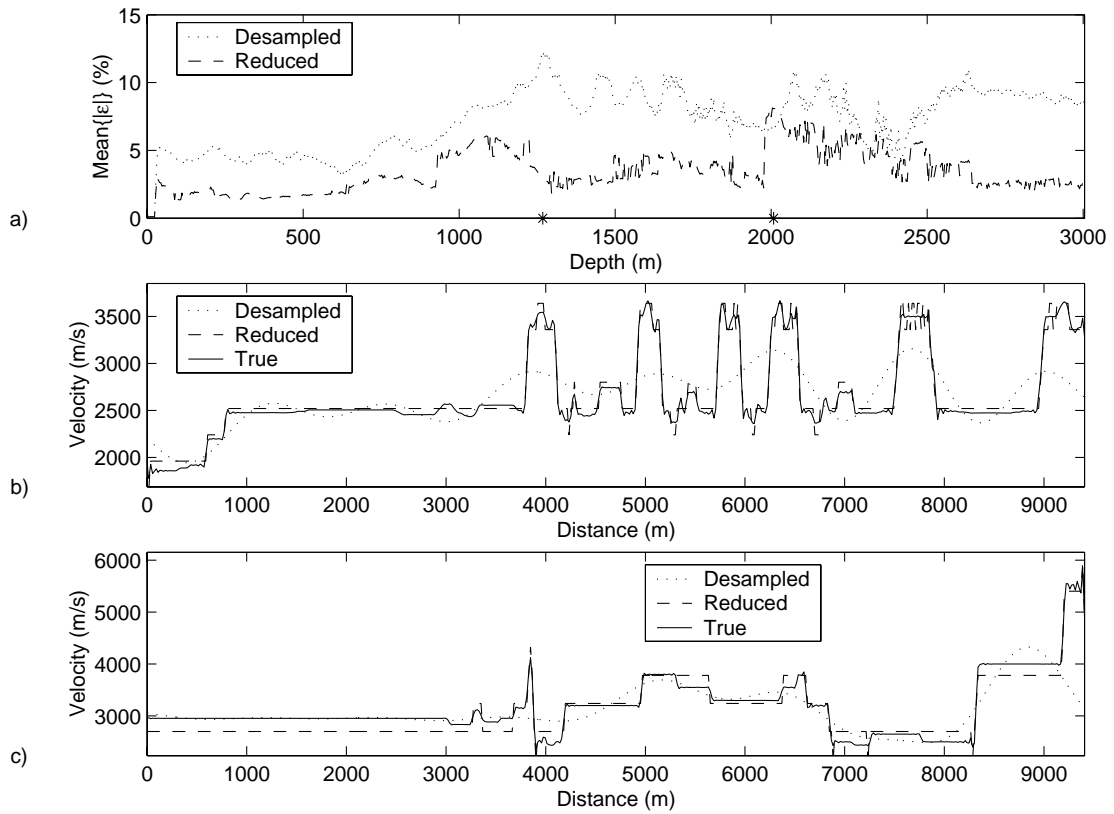


Figure 10. Average positioning error as a function of depth for similar computational cost. a) The dotted curve is the average error corresponding to the desampled velocity field of Figure 8, and the dashed curve is the error corresponding to the reduced velocity field of Figure 6. b) Velocity profile corresponding to 1260m depth. c) Velocity profile corresponding to 2020m depth.

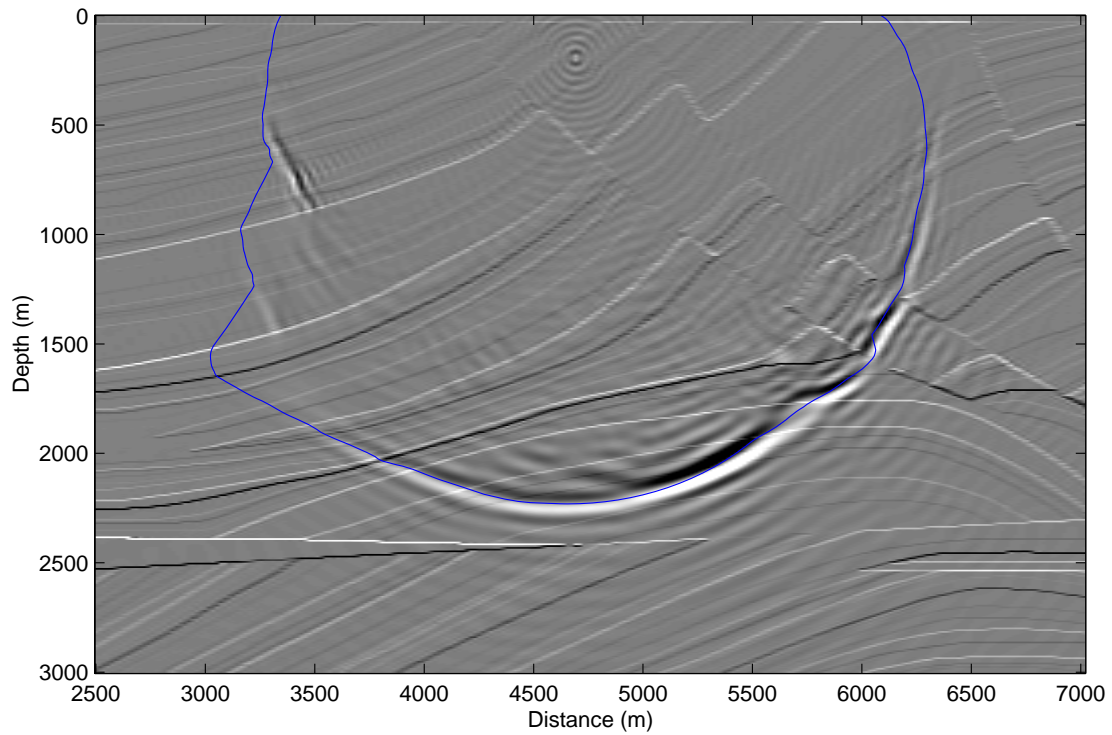


Figure 11. Snapshot of the propagating wavefield (uncorrected) based on the reduced model of Figure 6. The location of the impulse is distance 4670m and depth 195m, and the elapsed time is 0.82ms. i For comparison between Figures 11, 12, 13 and 14 the corresponding contour from a travelttime map of Figure 5 is plotted as well as the normal incidence reflectivity.

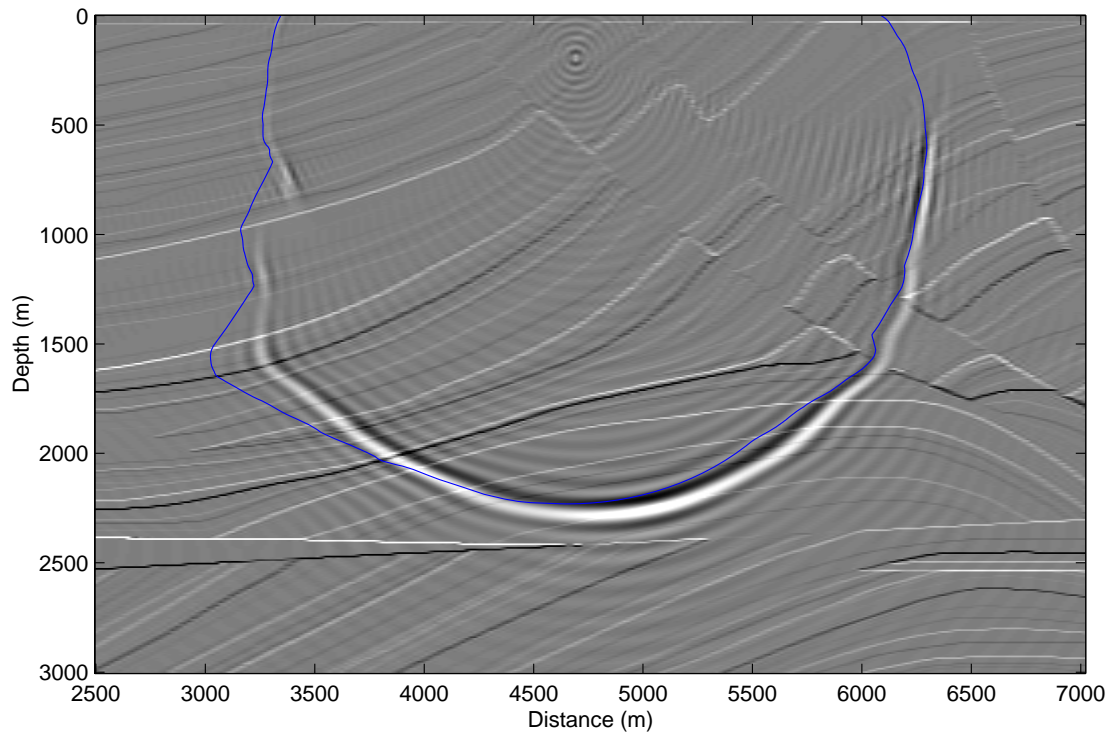


Figure 12. Snapshot of the propagating wavefield (uncorrected) based on the desampled model of Figure 8.

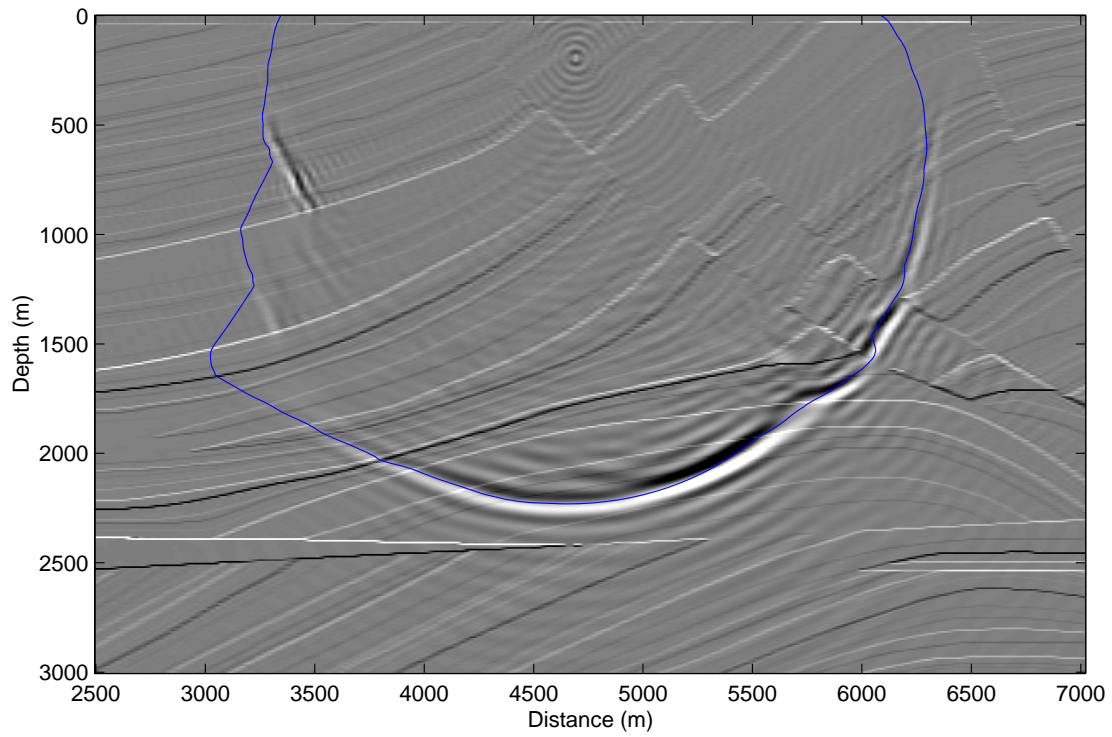


Figure 13. Snapshot of the propagating wavefield (corrected) based on the reduced model of Figure 6.

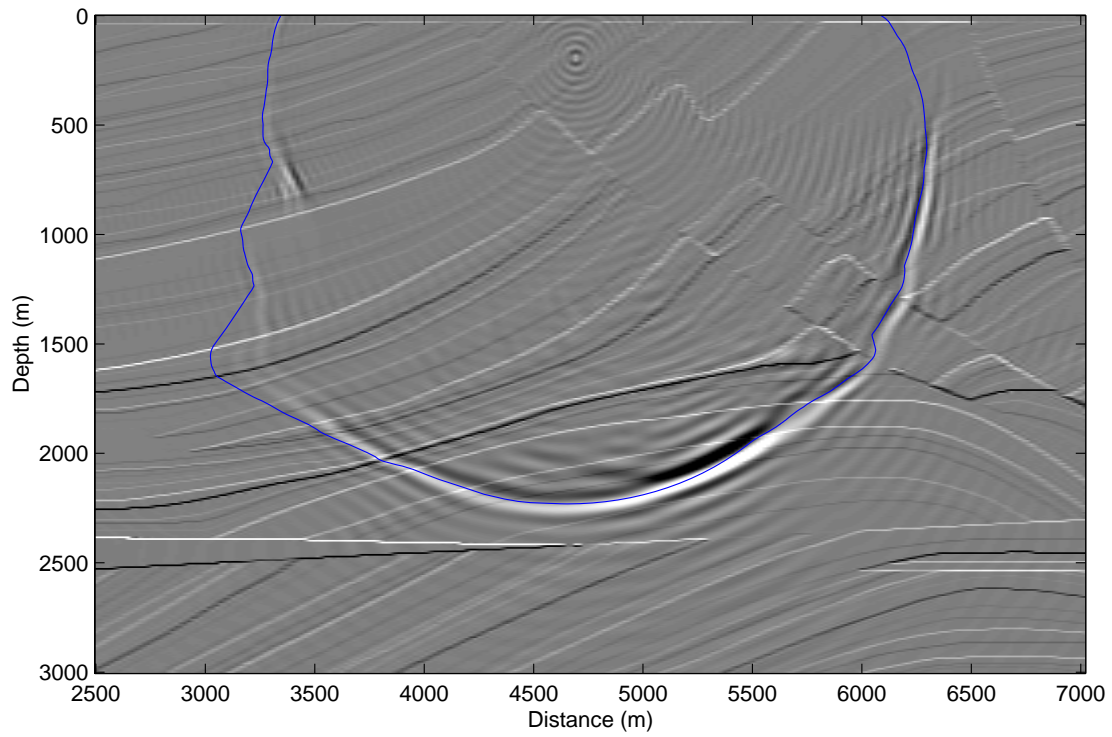


Figure 14. Snapshot of the propagating wavefield (corrected) based on the reduced model of Figure 8.

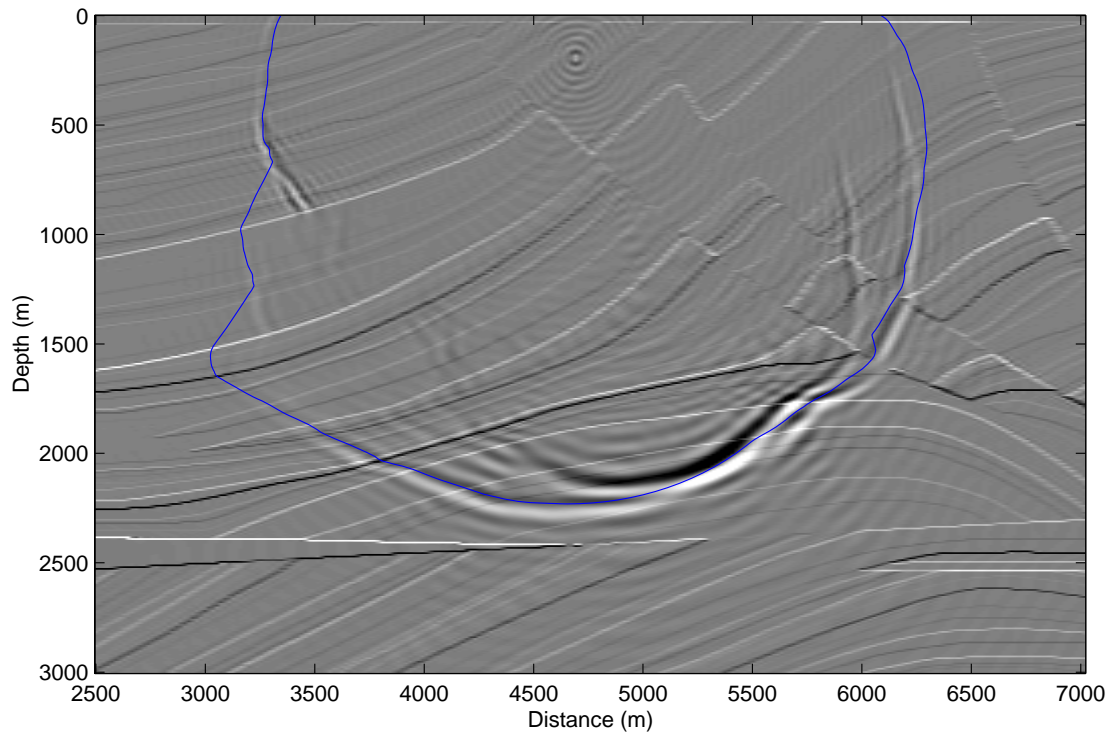


Figure 15. Snapshot of the propagating wavefield based on the phase-screen operator.

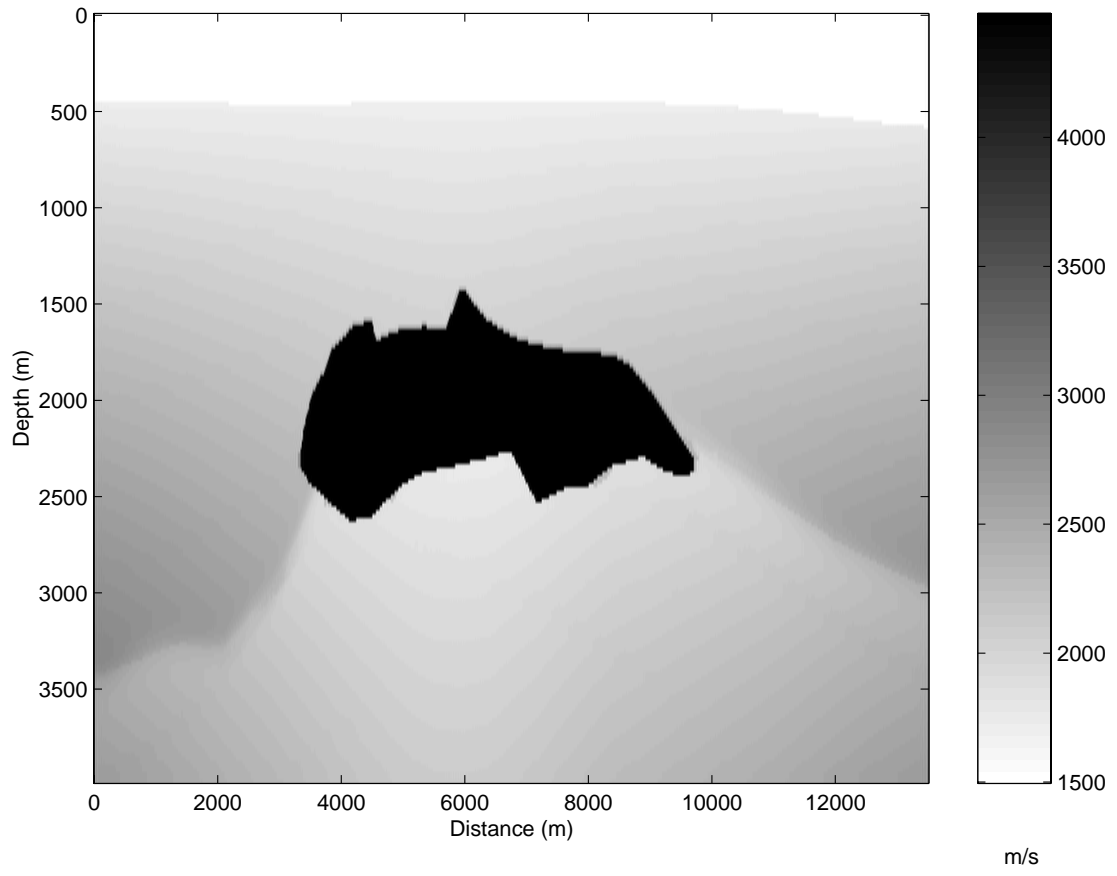


Figure 16. SEG salt model.

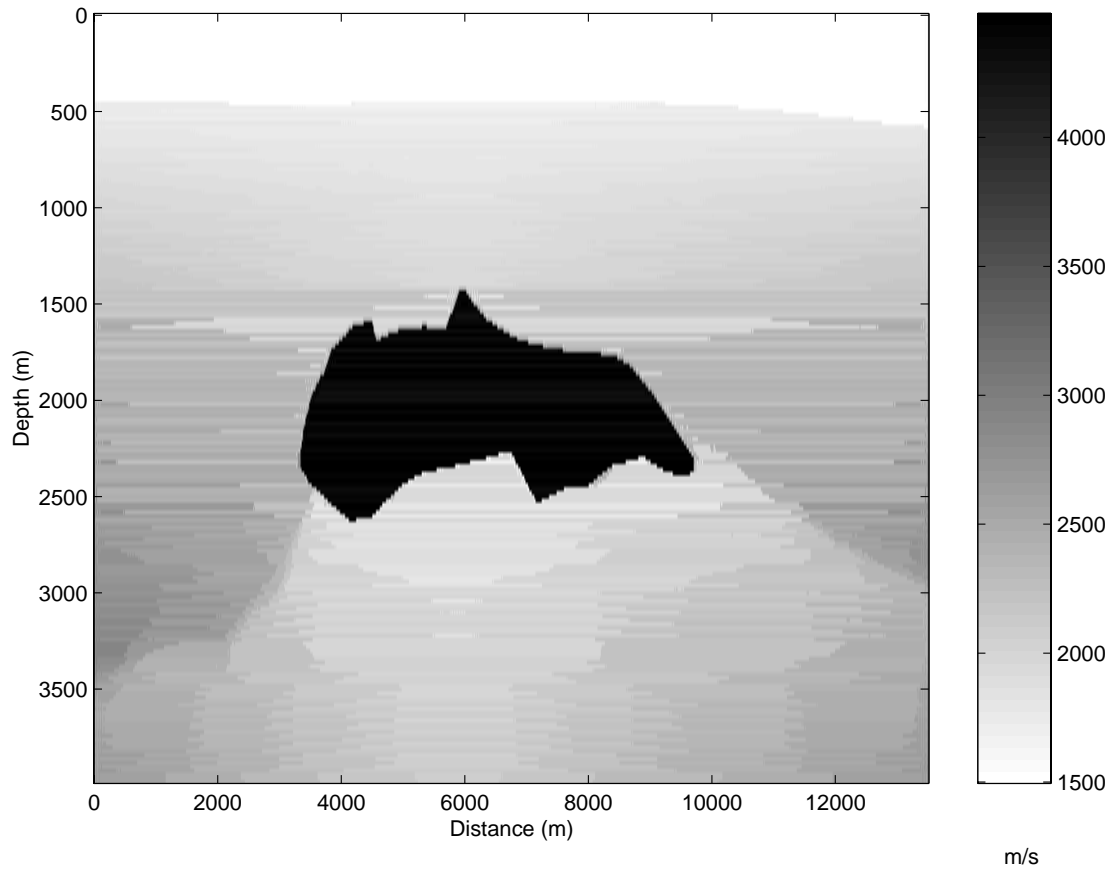


Figure 17. Salt model reduced to 10 unique velocity values along the lateral coordinate.

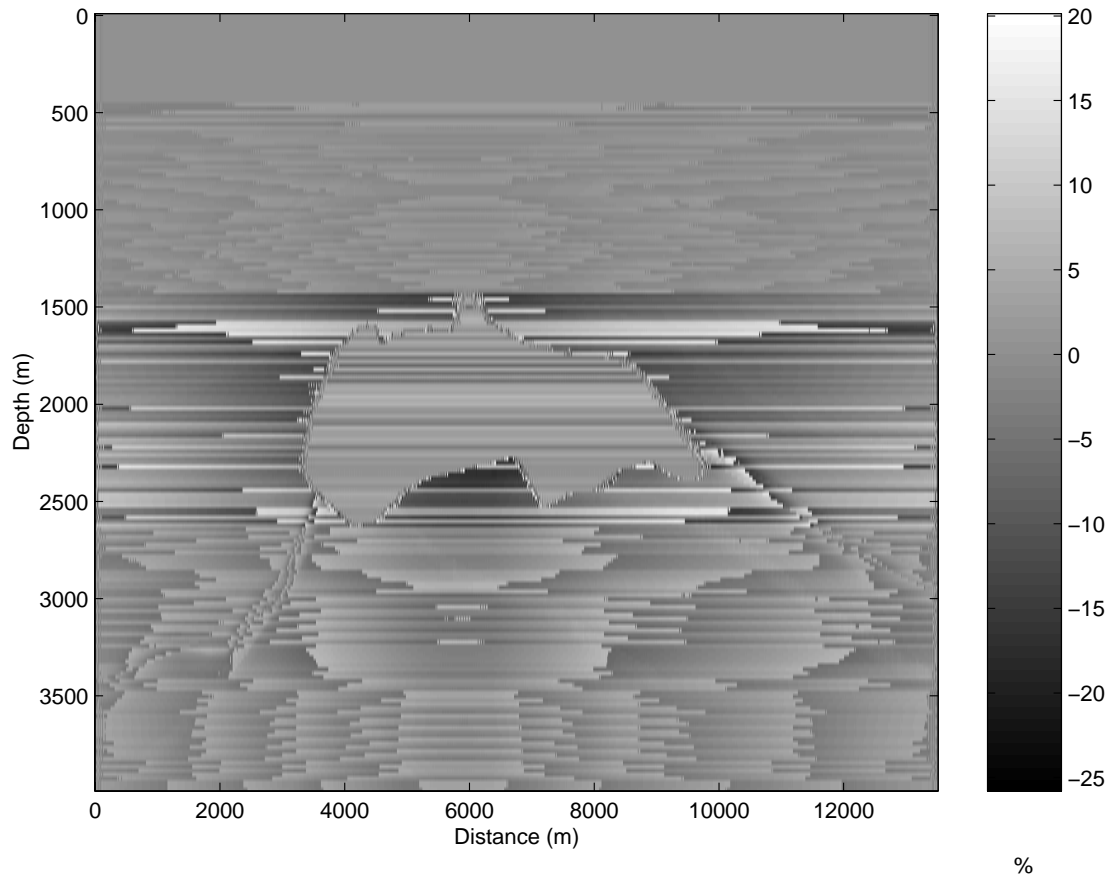


Figure 18. Positioning error associated with the reduced model of Figure 17. Grays represent absolute value of positioning error in percent for waves incident at 45 degrees.

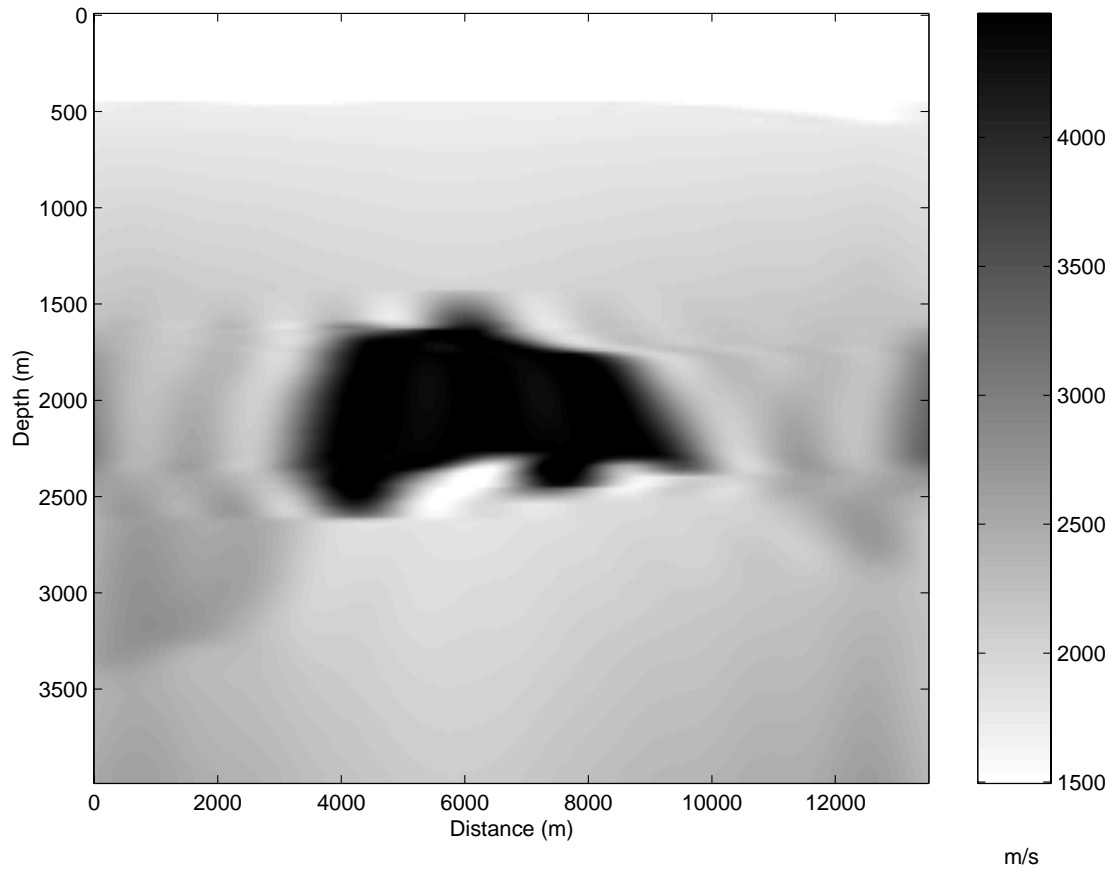


Figure 19. Salt model desampled to 8 velocity locations along the lateral coordinate.

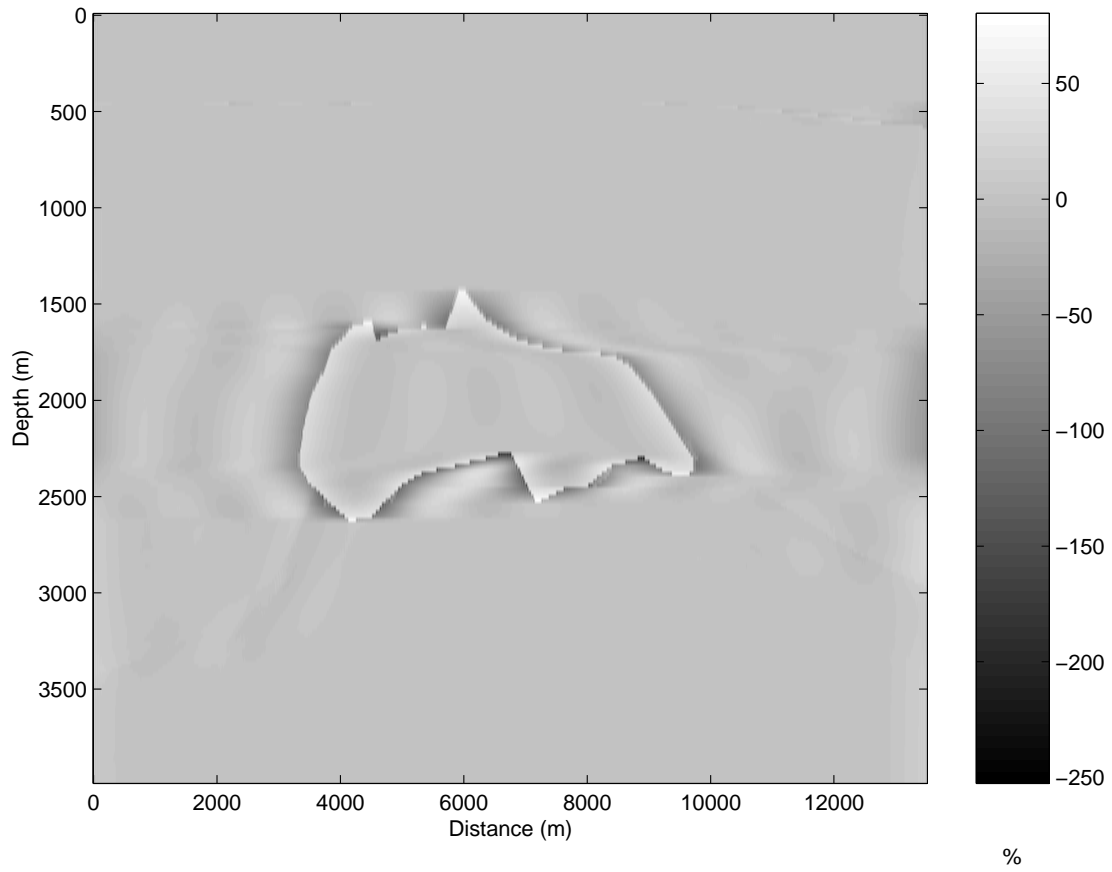


Figure 20. Positioning error associated with the desampled model of Figure 19. Grays represent absolute value of positioning error in percent for waves incident at 45 degrees.

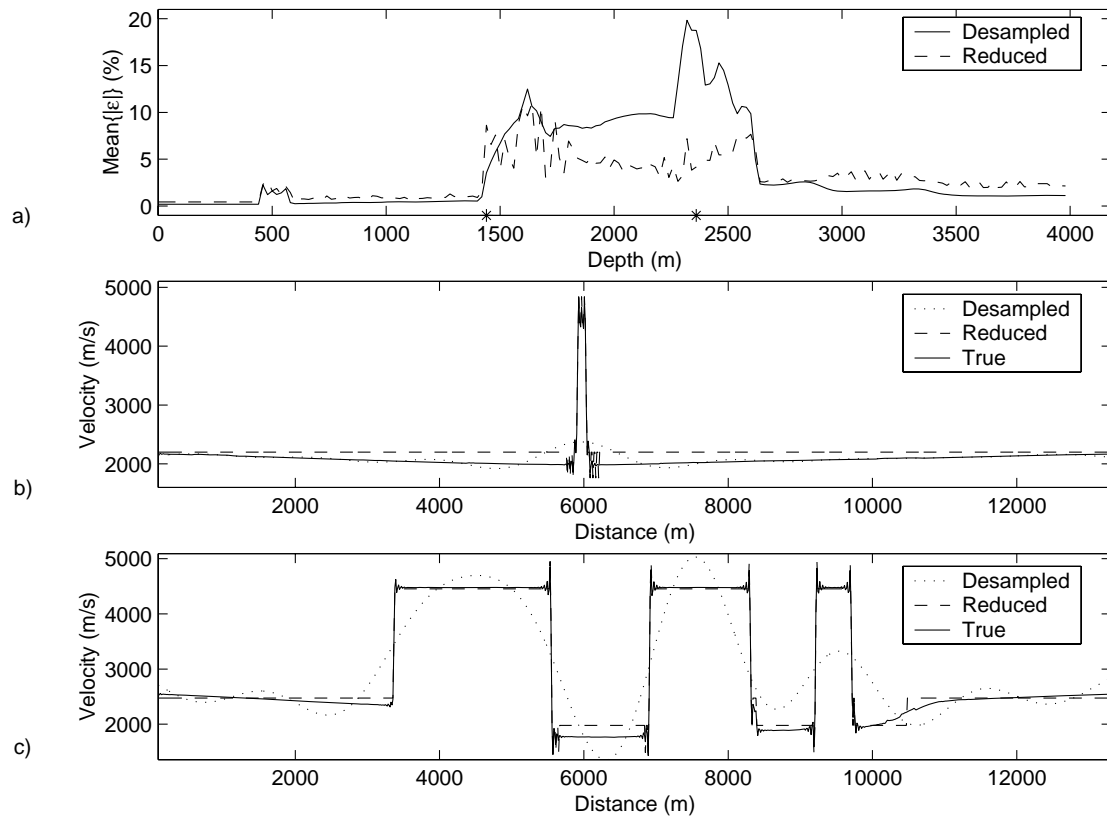


Figure 21. Average positioning error as a function of depth for similar computational cost. a) The dotted curve is the average error corresponding to the desampled velocity field of Figure 19, and the dashed curve is the error corresponding to the reduced velocity field of Figure 17. b) Velocity profile corresponding to 2370m depth. c) Velocity profile corresponding to 1460m depth.

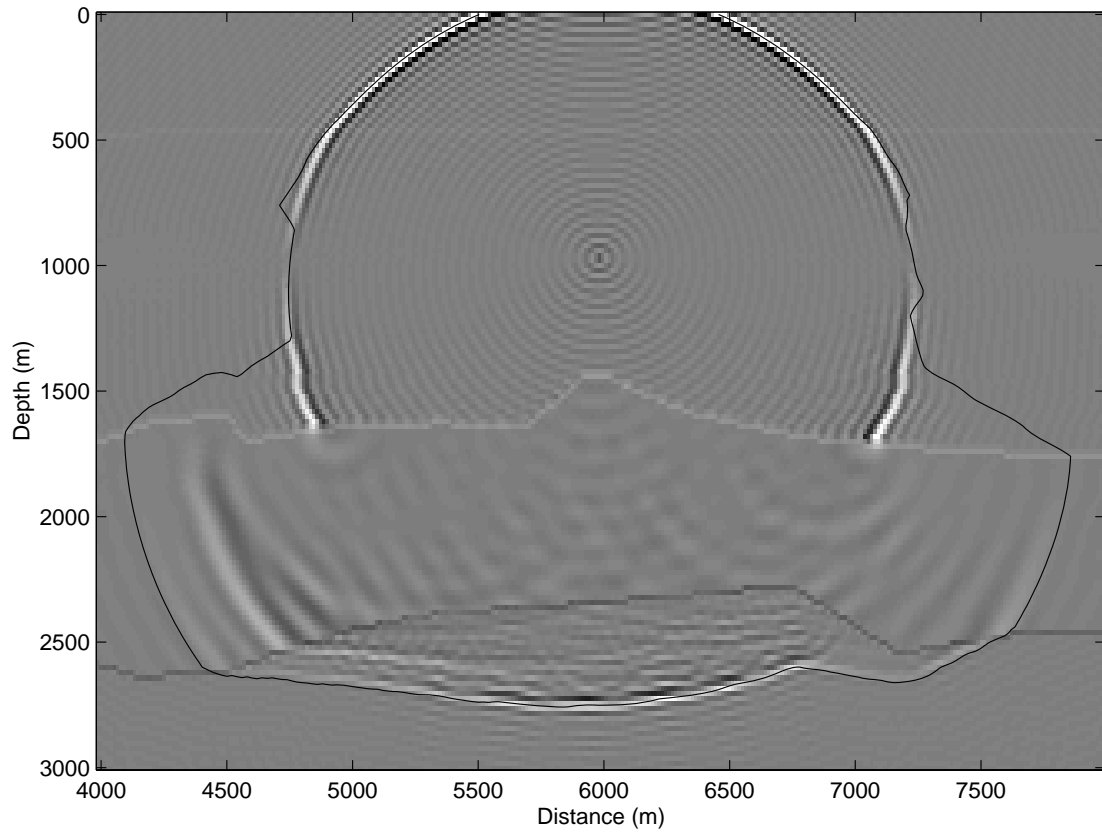


Figure 22. Snapshot of the propagating wavefield (uncorrected) based on the reduced model of Figure 17. The location of the source is 6000m distance and 1000m depth, and the elapsed time is 0.59ms. For comparison between Figures 22, 23, 24 and 25 the corresponding contour from a travelttime map of Figure 16 is plotted as well as the normal incidence reflectivity.

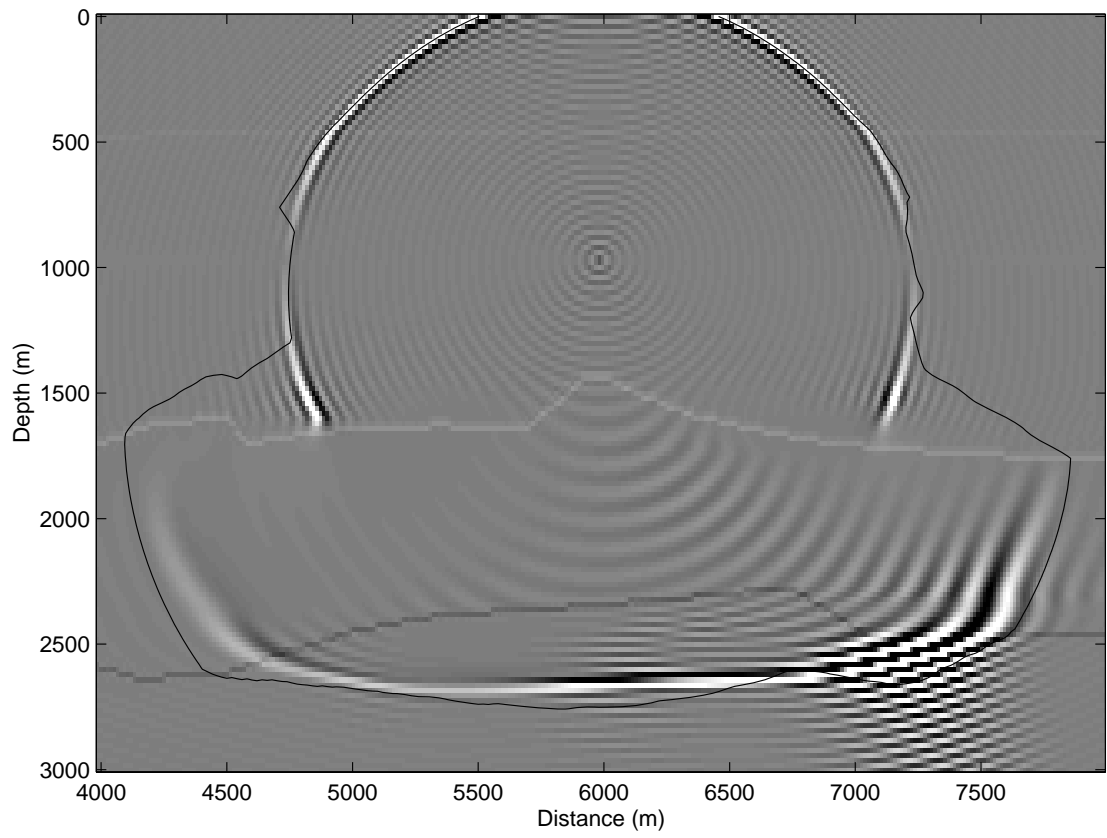


Figure 23. Snapshot of the propagating wavefield (uncorrected) based on the desampled model of Figure 19.

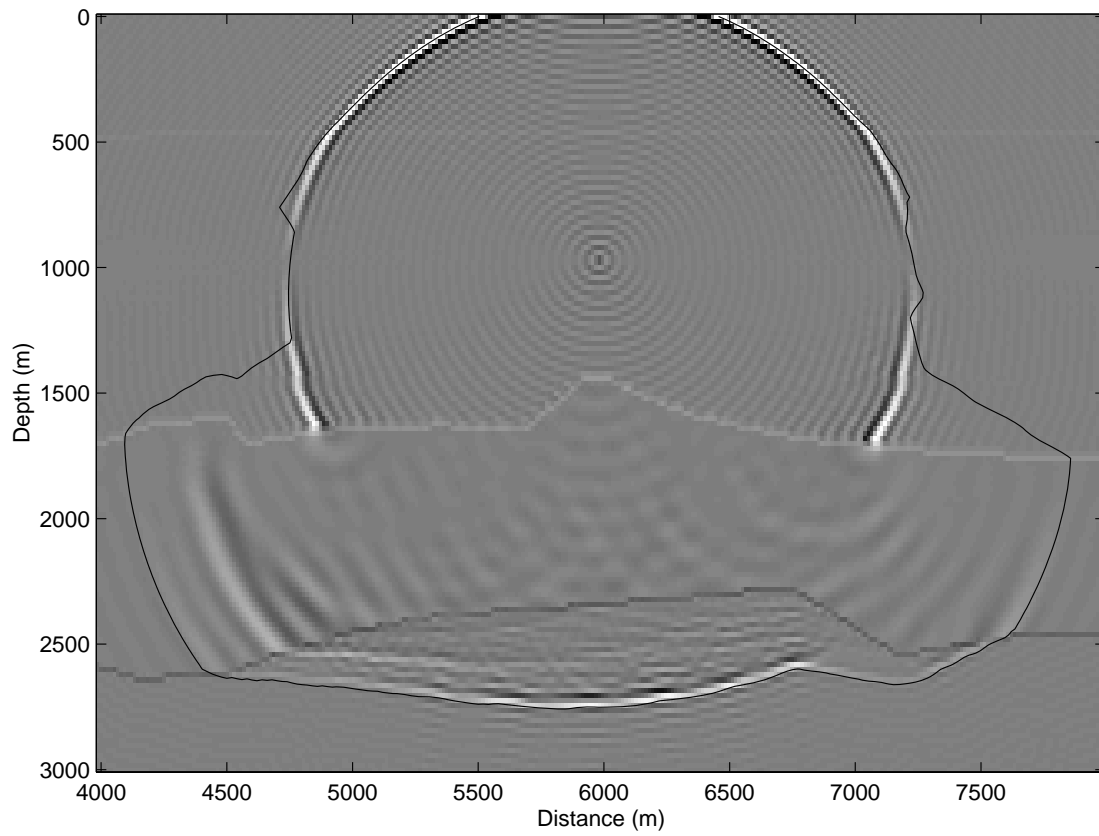


Figure 24. Snapshot of the propagating wavefield (corrected) based on the reduced model of Figure 17.

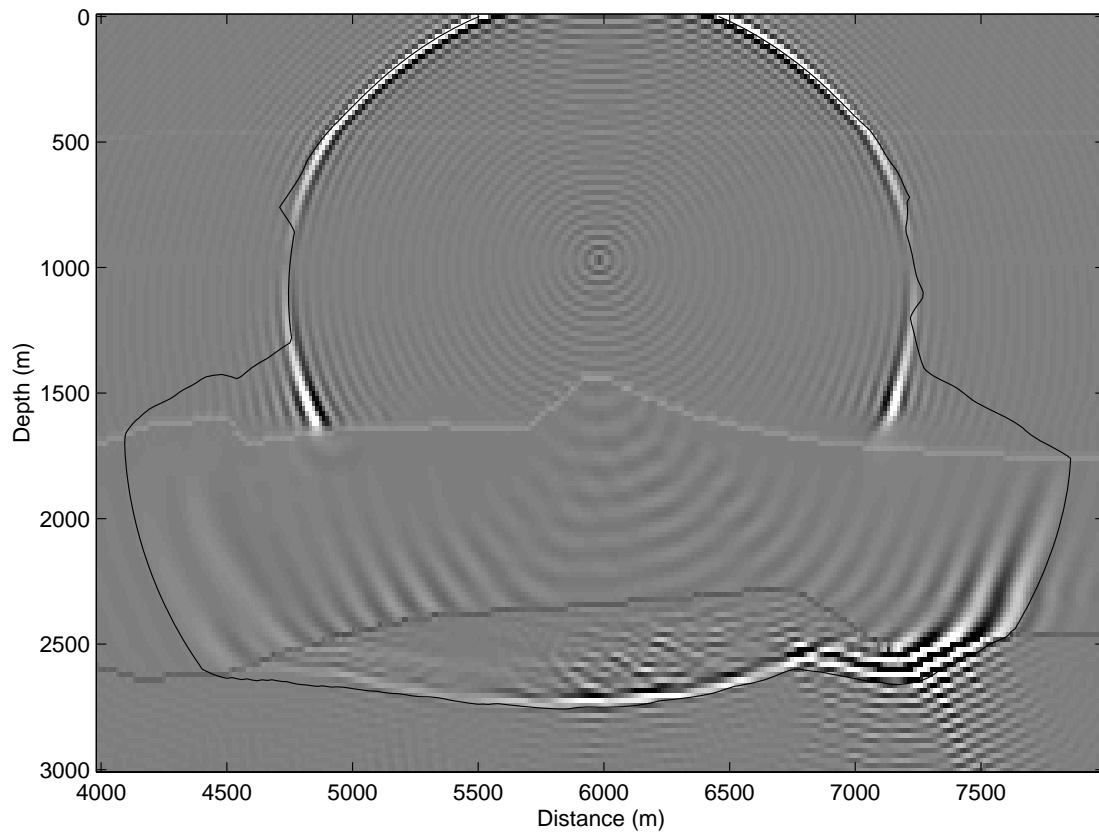


Figure 25. Snapshot of the propagating wavefield (corrected) based on the reduced model of Figure 19.

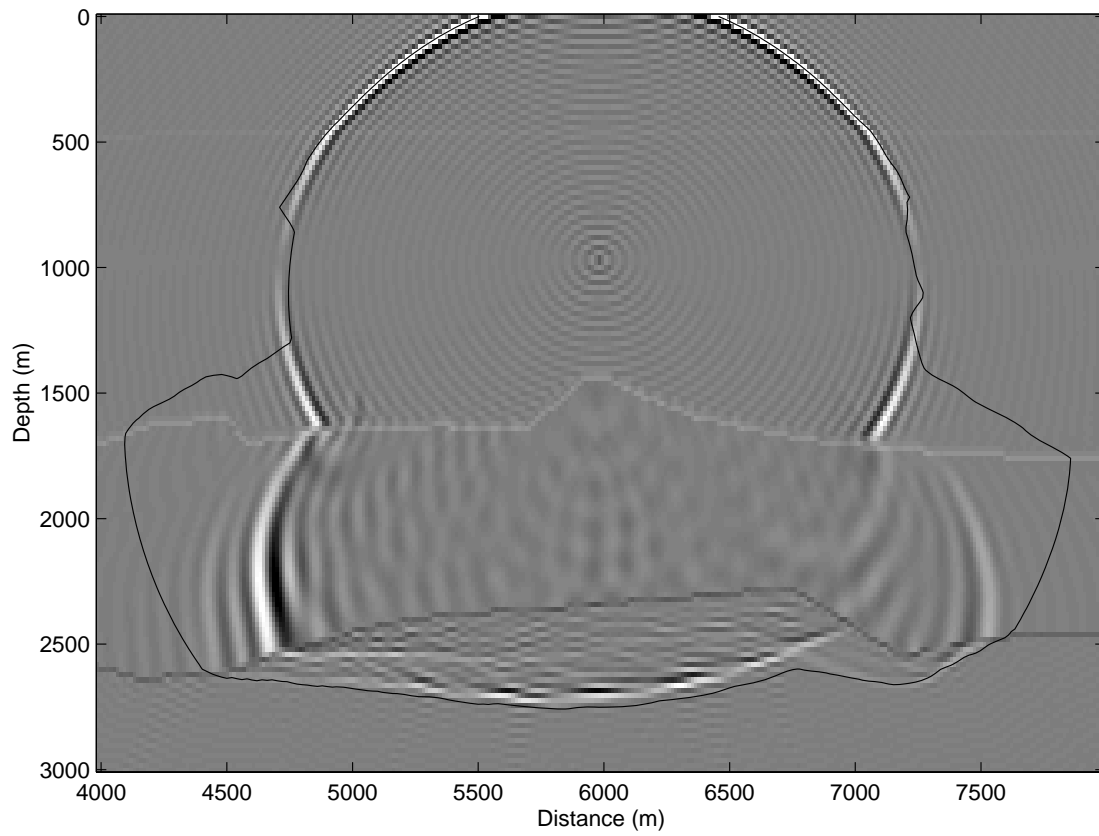


Figure 26. Snapshot of the propagating wavefield based on the phase-screen operator.